Desalination and Water Treatment
www.deswater.com

doi: 10.5004/dwt.2019.23727

150 (2019) 38–48
May

Modeling and experimental research on the formation of the super-gravity vacuum/low-pressure region for seawater desalination

Xiaolong Zang[a], Qingfen Ma[a,*], Kaier Liang[a], Hui Lu[b,*]

[a]*College of Mechanical and Electrical Engineering, Hainan University, Haikou, Hainan 570228, China, emails: mqf0920@163.com (Q. Ma), 494831387@qq.com (X. Zang), 1165342311@qq.com (K. Liang)*
[b]*Institute of Environment and Plant Protection, Chinese Academy of Tropical Agriculture Sciences, Haikou, Hainan 571101, China, email: aaaluhui@163.com (H. Lu)*

Received 12 July 2018; Accepted 31 December 2018

ABSTRACT

Seawater desalination is a promising solution to water scarcity especially for the coastal area. Super-gravity vacuum flash (SGVF) is a novel desalination technique we proposed previously, with a lot of advantages and suitable to be driven by the renewable energy source. The formation of the SGV or low-pressure circumstance is the precondition of this technique, thus the practical means of which are investigated in virtue of the numerical simulations and experimental tests. By analyzing the characteristics of the fluid field necessary for SGV formation, three driving modes of SGVE (SGV evaporator), candidate practical means, are proposed. The simulating results based on the built CFD model show that the dual-wall rotating mode is the best practical mean. The parameter influences are investigated, in good agreements with the theoretical calculations, and also some suggestions for SGVE design and operation are proposed. A test platform is set up to verify that the dual-wall rotating mode is feasible for the formation of the SGV or low-pressure circumstance experimentally. The pressure drop during the formation of the super-gravity low- pressure region is monitored, in good consistence with the simulating and theoretical predictions. At the experimental conditions, the minimal monitored absolute pressure can achieve 8.9 kPa, in the same order as the saturated pressure of water at ambient temperature. The tested energy consumption for driving SGVE is relatively small and would not cause the extra power consumption for the decreasing power requirement of the auxiliary vacuum pump. Furthermore, a novel desalination process, SGV-MD is proposed and analyzed, which is considered more suitable for seawater desalination and renewable energy utilization.

Keywords: Super-gravity; Vacuum/low pressure distillation; CFD simulation; VMD

1. Introduction

Water scarcity is often considered as one of the greatest challenges in the twenty-first century. According to the United Nation's World Health Organization, this issue is further aggravated by the mounting figure of human population combining with the soaring demand for food and other necessities. It is estimated that water withdrawal is growing twice the rate of human population by 2050 (FAO, 2016) [1]. Thus, it is crystal clear that water scarcity needs to be addressed urgently. Desalination is often considered one of the promising ways to obtain fresh water by desalinating brackish or abundant seawater [2], especially among coastal areas such as Saudi Arabia and Israel where desalination has become a non-negligible source to supply fresh water [3]. In a variety of seawater desalination technologies, multi-stage flash (MSF) and reverse osmosis (RO) are primarily adopted, occupying over 85% of current desalinated water production [4].

In MSF process, water is evaporated and then separated from seawater through a series of multi-stage flash

* Corresponding authors.

distillation. It is estimated that multi-stage flash distillation units produce approximately 21% of all desalinated water in the world [4]. Depending on the temperature of the working environment, the evaporation capacity in all the stages can reach 15% of the flowing water through the system. One advantage of MSF lies in the source of its energy since power plants are usually coupled in cogeneration configuration providing energy via the form of waste heat which is suitable for constructing large or ultra large desalination units. Apart from that, its low requirement for feed water quality makes it more appearing for Gulf States where seawater is severely polluted by oil industry [5].

Nonetheless, concerning cost and energy consumption, RO is the most favorable one that accounts for 65% of total desalinated water [4]. In RO, a semi-membrane is deployed to remove salts from seawater with an applied pressure to overcome the osmotic pressure. During the RO process, membrane pollution is often concerned which directly affects the efficiency of RO units [6]. Still, it is predictable that RO will occupy an increasingly important position due to its positive significance. The Ashkelon sea water RO desalination plant in Israel has become the current largest desalination plant in the world [7].

Other kinds of desalination technologies were also explored with different principles. In multi-effect distillation (MED), a series of evaporators are adopted to evaporate seawater using the steam in the previous evaporator as the heat source, and simultaneously the steam is condensed into fresh water as final product [8]. Electro dialysis (ED) is a technology applying external electric field of direct current to selectively direct ions passing an exchange membrane [9]. These two technologies account for 7% and 3% of global desalinated water, respectively [4]. In addition, there are also several novel desalination processes developed in recent years including forward osmosis (FO) [10], membrane distillation (MD) [11,12], humidification- dehumidification (HDH) [13], capacitance deionization (CDI) [14], gas hydrates (GH) [15] and freezing [16], which are still under research and have good perspective.

Over the last thirty years, the cost of the desalination technology has been reduced by lowering the energy consumption and optimizing the design. The cost of the desalination technology is primarily affected by the capital investment and energy cost, while other factors include operation and maintenance cost, water source salinity, energy source availability, the plant size, land cost, the government subsidy etc [17]. Although, the aforementioned commercial desalination technologies have been developed to a relatively mature stage and 88.6 million cubic meters of freshwater are produced by over 19,000 desalination plants and projects per day [18], new concern emerges due to the environment impact caused by high energy consumption, pollution, and greenhouse gas emission [19]. Therefore the renewable clean energy which is either environment-friendly or inexhaustible is expected to take over increasing share of energy supply. Currently, due to the high cost of harvesting renewable energy resources and their high level requirements of technology and infrastructure, the adoption of renewable energy in desalination systems are inefficient compared with the fossil fuel. However, a further development and research will succeed in reducing cost of the renewable energy utilization in the near future [20]. Among frequently adopted renewable energies such as solar photovoltaic (PV), nuclear energy, wind power, etc., 70% of renewable energy desalination plants are powered by solar energy [21]. However, massive land areas are required to collect solar radiation and thus wind energy or hybrid renewable energy is often preferred in coastal areas both commercially and technically and has been proven to be highly efficient [20,22–24].

For remote areas with inability to supply high back pressure and keep constant maintenance, RO is no longer a suitable option for renewable energy utilization and water supply. The adopted desalination process needs to discharge less chemical waste, be easily operated, provide high quality water, and also harbor fine compatibility with wind power or the hybrid renewable energy system. Mechanical vapor compression (MVC) is the major thermal desalination process integrated with wind power [25]. However, the high operating temperature might give rise to many issues particularly the thermal energy loss and the seawater scaling. Vacuum or low-pressure distillation converting water to vapor at the ambient/low temperature could effectively reduce the thermal energy loss and alleviate the scaling. To save the extra electricity consumption for maintaining vacuum or low-pressure circumstance, a natural vacuum technique (NVD) was developed and studied by Midilli [26], Al-Kharabsheh and Goswami [27,28] in which vacuum environment is created by the natural means (gravity and atmospheric pressure). Nevertheless, the necessary equipment height could render problems such as space requirement, maintenance and operational issues.

Hence, we proposed a "super-gravity" vacuum flash (SGVF) technique for seawater desalination or water purification, in which the vacuum environment is obtained not only by the vacuum pump but also combing the SGV equipment with much more compact structure than the NVD equipment [29]. The vacuum pump load can be decreased effectively, and meanwhile, the decrease in equipment height makes the operation and maintenance much easier. In the previous published work, the SGVF process is conceptually designed, each key unit is theoretically calculated and analyzed, and also the potential for SGVF process to achieve the desalination purpose is predicted [29]. Since the formation of the SGV or low-pressure circumstance is the precondition of this technique, the practical means of which are investigated in virtue of the numerical simulations and experimental tests in this paper, i.e., the focus is to explore the practical means to obtain the necessary vacuum/ low-pressure environment for water evaporation. CFD models for SGV formation will be built to compare and screen out the suitable means, and the results will be verified by series of experiments, based on which more suitable super-gravity low-pressure desalination process with better prospects for development will be proposed.

2. Alternative schemes for the SGV formation

According to the formation theory of SGV [29], the vacuum/low- pressure (equal to saturated vapor pressure of fluid at the ambient temperature, approaching vacuum) region can be formed around the center of the flow field which satisfies the following two conditions: (1) The flow

field is geometrically like a rotary cylindrical body with the free surface at the outlet greater than the minimum height z_o to avoid the entrance of external air causing damage to the low pressure environment; (2) After the rotated fluid become relatively static with the cylinder, the internal rotational velocity distribution should be stable without any local acceleration, deceleration or abrupt change.

From the stationary state to the SGV state, the SGV formation is predicted to undergo the following processes. The fluid is introduced into a vessel with the above required geometry, and then rotates together with the vessel at a constant rotational velocity under the action of the viscous force. Due to the centrifugal force, the peripheral fluid appears to rise along the wall of the vessel and the fluid pressure around the center gradually decreases until it is lower than the saturated vapor pressure at the ambient temperature. At this moment, the liquid begins to evaporate and the super-gravity low-pressure region gradually expands from the center. When the rotational velocity approaches stable state, the liquid reaches in a rotational equilibrium in relative to the vessel, the SGV region reaches its maximum volume and no longer changes.

According to the earlier description, whether the SGV region or low pressure environment can be formed greatly depends on the rotating mode of the SGVE (SGV evaporator, i.e. the rotating vessel) which will affect the complexity of the actual implementation as well. Fig. 1 shows the simplified geometry of a SGVE, with an overflow weir to offer a higher free surface preventing the entrance of external air. Based on this shape of SGVE, three alternative practical means for the SGV formation, i.e. three driving modes are proposed as follows:

(1) *Inner-wall rotating mode*. The inner-wall is shown in Fig.1 in red color. In this rotating mode, the rotating parts are few in number and light in weight, and it is convenient for arrangement of external static interfaces such as the seawater inlet and brine outlet as the outer-wall (as shown in Fig. 1 in blue) remains static all along. The inadequacies are that it is hard to guarantee the uniformity of the overflow weir gap, and that the limited rotational driving area might influence the acceleration of fluid and the formation of SGV region.
(2) *Outer-wall rotating mode*. Although, the number of rotating parts is the same as the first mode, the rotational driving area and the weight are both increases. As the inner-wall remains static all along, it is also convenient for the arrangement of external static interfaces. Similar to the first mode, the uniformity of the overflow weir is not easily to be guaranteed either.
(3) *Dual-wall rotating mode*. The inner and outer walls rotate synchronously in this mode. The rotational driving area is the largest among the three modes while the rotating parts are most in number and heaviest in weight. Meanwhile, the uniformity of the overflow weir gap can be easily guaranteed through the integrated structure design. However, as there is no static part, dynamic connection and sealing between SGVE and external interfaces could result in more complex structure, raising the design difficulties and the device cost.

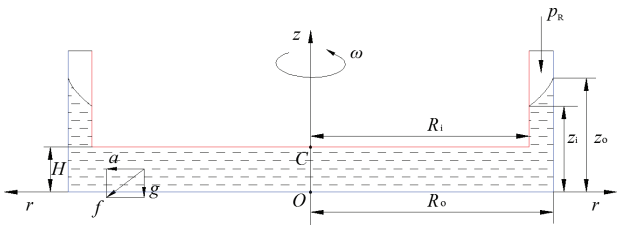

Fig. 1. Simplified geometry of a SGVE.

3. CFD model and simulations

Based on the axisymmetric characteristics of the flow field required for the SGV formation, the 3D geometrical model can be simplified into a 2D axisymmetric rotating model. The fresh water is adopted as the simulating medium and the conversion of driving mode is fulfilled by altering the boundary-condition setting. The practical feasibilities of different driving model are compared by investigating the volume of the formed SGV region, based on which optimal driving mode, optimal practical means for SGV formation, is screened out. Furthermore, a series of simulations at the optimal driving mode are conducted to investigate the influences of key operational and structural parameters on SGV formation and to verify the previously proposed theory of SGV formation.

3.1. CFD model

3.1.1. Geometric model and mesh

Table 1 explains the primary operational and structural parameters of SGVE shown in Fig. 1, from which other parameters can be derived. The wall thicknesses of SGVE are all neglected, and the overflow weir gap $L = R_O - R_i$. The sum of H and H_y should greater than z_O, which is determined by structural operating parameters [29]. The fluid domain is meshed by Map scheme to obtain the quadrilateral structure mesh. In order to improve the simulation accuracy, the pressure outlet is locally refined. The number of grid points along the x and r direction is related to the size of the geometrical model and varies with the major structural parameters.

Table 1
Primary operational and structural parameters of SGVE.

Structural parameters (m)				Operating parameters			
Out-wall diameter	Evaporation chamber height	Overflow weir gap	Overflow weir height	Rotational speed	Outlet pressure	Temperature	Saturated vapor pressure
Ro	*H*	*L*	H_y	ω (rad/s)	p_R (Pa)	*T* (K)	p_s (Pa)

In specific, along the x direction the number of grid points is determined by H and H_y with uniform mesh space of 8 mm. The number of grid points along the r direction is determined by R_O and L, with mesh space of 8 mm and 1.5 mm respectively. The near wall mesh is refined and the standard wall function [30] is employed to simulate the boundary layer flow. As advised by the user manual of the CFD code and the shared experiences of many users, the near wall grids of all the walls are refined until that the first grid's y* [30] of all the walls fall into the recommended range, 11.225 to 300. The finally size of the mesh is determined by the independence analysis. A mesh example of simulated fluid domain of SGVE is shown in Fig. 2.

3.1.2. Flow equations

Flow equations include differential equations of continuity, kinematics, and turbulence. Eq. (1) is the continuity equation for 2D axisymmetric geometry, where x is the axial coordinate, r the radial coordinate, v_x the axial velocity, v_r the radial velocity, and ρ the freshwater density.

$$\frac{\partial \rho}{\partial t}+\frac{\partial}{\partial x}\left(\rho v_x\right)+\frac{\partial}{\partial r}\left(\rho v_r\right)+\frac{\rho v_r}{r}=0 \tag{1}$$

For 2D axisymmetric geometries, the axial and radial momentum conservation equations are given by Eqs. (2) and (3),

$$\begin{aligned}&\frac{\partial}{\partial t}\left(\rho v_x\right)+\frac{1}{r}\frac{\partial}{\partial x}\left(r\rho u_x v_x\right)+\frac{1}{r}\frac{\partial}{\partial r}\left(r\rho v_r v_x\right)\\&=-\frac{\partial p}{\partial x}+\frac{1}{r}\frac{\partial}{\partial x}\left[r\mu\left(2\frac{\partial v_x}{\partial x}-\frac{2}{3}\left(\nabla\cdot\vec{v}\right)\right)\right]\\&+\frac{1}{r}\frac{\partial}{\partial r}\left[r\mu\left(\frac{\partial v_x}{\partial r}+\frac{\partial v_r}{\partial x}\right)\right]+F_x\end{aligned} \tag{2}$$

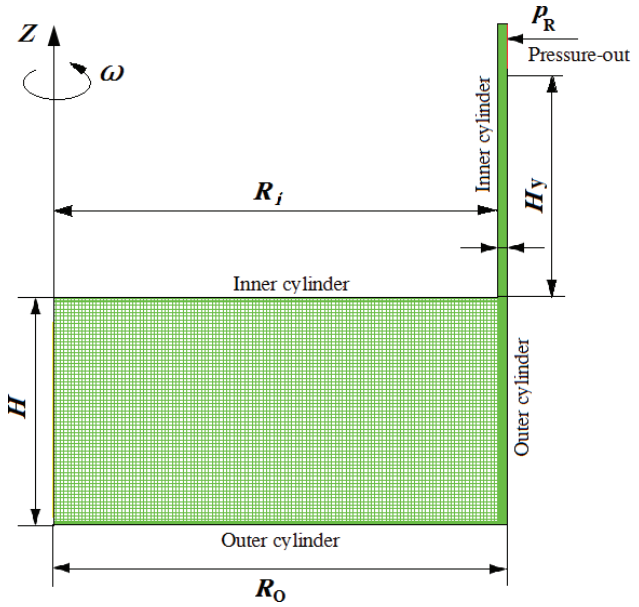

Fig. 2. A mesh example of simulated fluid domain of SGVE.

$$\begin{aligned}&\frac{\partial}{\partial t}\left(\rho v_r\right)+\frac{1}{r}\frac{\partial}{\partial x}\left(r\rho u_x v_x\right)+\frac{1}{r}\frac{\partial}{\partial r}\left(r\rho v_r v_r\right)\\&=-\frac{\partial p}{\partial r}+\frac{1}{r}\frac{\partial}{\partial x}\left[r\mu\left(\frac{\partial v_r}{\partial x}+\frac{\partial u_x}{\partial r}\right)\right]\\&+\frac{1}{r}\frac{\partial}{\partial r}\left[r\mu\left(2\frac{\partial v_r}{\partial r}-\frac{2}{3}\left(\nabla\cdot\vec{v}\right)\right)\right]\\&-2\mu\frac{v_r}{r^2}+\frac{2}{3}\frac{\mu}{r}\left(\nabla\cdot\vec{v}\right)+\rho\frac{v_z^{\,2}}{r}+F_r\end{aligned} \tag{3}$$

where

$$\nabla\cdot\vec{v}=\frac{\partial v_x}{\partial x}+\frac{\partial v_r}{\partial r}+\frac{v_r}{r} \tag{4}$$

And v_z is the swirl velocity, p the fluid pressure, F_x and F_r are the components of the volumetric force in the corresponding direction. μ is the dynamic viscosity coefficient, which is considered as a constant for each phase.

The problem is axisymmetric with respect to geometry and flow conditions but still include swirl or rotation. It is important to note that while the assumption of axisymmetry implies that there are no circumferential gradients in the flow, there may still be non-zero swirl velocities. The tangential momentum equation for 2D swirling flows cab be written as Eq. (5).

$$\begin{aligned}&\frac{\partial}{\partial t}\left(\rho u_z\right)+\frac{1}{r}\frac{\partial}{\partial x}\left(r\rho u_x u_z\right)+\frac{1}{r}\frac{\partial}{\partial r}\left(r\rho u_r u_z\right)\\&=\frac{1}{r}\frac{\partial}{\partial x}\left[r\mu\frac{\partial u_z}{\partial x}\right]+\frac{1}{r^2}\frac{\partial}{\partial r}\left[r^3\mu\frac{\partial}{\partial r}\left(\frac{u_z}{r}\right)\right]-\rho\frac{u_r u_z}{r}\end{aligned} \tag{5}$$

The turbulence is simulated by standard k-ε model, and Eqs. (6) and (7) are the governing equations of the turbulent kinetic energy k and the dissipation rate ε respectively, where C_μ = 0.09, σ_ε =1.3, $C_{1\varepsilon}$ = 1.44, $C_{2\varepsilon}$ = 1.92, σ_k = 1.0; G_b is the production term caused by buoyancy, for incompressible fluids, G_b = 0; G_k is the production term of the turbulent kinetic energy k, which is caused by the mean velocity gradients and calculated by Eq. (8).

$$\frac{\partial(\rho k)}{\partial t}+\frac{\partial(\rho k u_i)}{\partial x_i}=\frac{\partial}{\partial x_j}\left[\left(\mu+\frac{\mu_i}{\sigma_k}\right)\frac{\partial k}{\partial x_j}\right]+G_k+G_b-\rho\varepsilon+S_k \tag{6}$$

$$\begin{aligned}&\frac{\partial(\rho\varepsilon)}{\partial t}+\frac{\partial(\rho\varepsilon u_i)}{\partial x_i}=\frac{\partial}{\partial x_j}\left[\left(\mu+\frac{\mu_i}{\sigma_\varepsilon}\right)\frac{\partial\varepsilon}{\partial x_j}\right]\\&+G_{1\varepsilon}\frac{\varepsilon}{k}\left(G_k+C_{3\varepsilon}G_b\right)-C_{2\varepsilon}\rho\frac{\varepsilon^2}{k}+S_\varepsilon\end{aligned} \tag{7}$$

$$G_k=\mu_i\left(\frac{\partial u_i}{\partial x_j}+\frac{\partial u_j}{\partial x_i}\right)\frac{\partial u_i}{\partial x_j} \tag{8}$$

3.1.3. Phase-change model

In the formation of the SGV region, water (at constant temperature) around the center of rotated SGV evaporator is subjected to a decreasing pressure, which will fall below the saturated vapor pressure. This process is exactly the same as the cavitation which is a process of rupturing the liquid by a decrease of pressure at a constant temperature. Thus the formation of the SGV region is simulated by the cavitation model originally developed by Singhal et al., [31]. In this model, the primary phase is liquid, and the generated vapor takes the form of small bubbles. The liquid-vapor interface is represented by the volume fraction of vapor or water which is calculated based on the proper account of bubble growth and collapse according to the bubble dynamics. The detail of above theories can be found in lit [31].

3.1.4. Boundary condition settings

The boundary conditions include Pressure-out, wall and axis with specific position shown in Fig. 1. Inner-wall and outer-wall are set separately to facilitate the static/rotating wall setting to realize the simulation of different driving mode, i.e. inner-wall rotating while outer-wall keeping static, inner-wall keeping static while outer-wall rotating, and both two walls rotating.

3.1.5. Initialization of fluid field

Although, initial effect should theoretically disappear if the simulation time is long enough, poor initial conditions very often lead to an unrealistic pressure field and unexpected cavitation zones, which, once present, are then usually very difficult for the model to correct. To eliminate the influence of the initial effect and to obtain more accurate simulation results, our simulation follows the procedures below. First, set near zero relaxation factors for the vaporization mass and for density, and increase them to reasonable values after a sufficient number of iterations. Second, obtain a converged / near-converged solution for a single phase water flow, and then switch on the cavitation model.

3.1.6. Solution strategy

Discretization of the above equations employs the finite-volume approach, with the solution being obtained by a pressure-based approach. Considering that an intense phase change occurs in the process of SGV formation, the first-order upwind scheme is employed, and the literation is carried out based on the transient scheme with the maximal time interval of 0.01 s. For each time step, the solutions are converged to normalized RMS residuals of the order of 10^{-3} or lower. The stability of the system is measured by monitoring the pressure at the critical position and the mass flow rate at the outlet. When the pressure is constant and the exit mass flux is approaching 0, the system reaches a steady state and the calculation is completed.

3.2. Simulation results and discussions

3.2.1. Comparison of different driving modes

Fig. 3 shows the volume fraction of water at three different driving modes, based on which the volume of SGV region is calculated equal to that of the vapor region in blue color. Comparing the volume of SGV region, the maximal appears in the dual-wall rotating mode, and the minimal in the inner-wall rotating mode. When the inner and outer wall rotates at the same time, the rotational speeds of the inner and outer walls are transmitted to the fluid through the viscous force, and the fluid is accelerated gradually and theoretically achieves nearly the same rotational speed as the inner and outer walls. When the inner or outer wall rotates, there will be a velocity gradient (from the maximum rotational speed to zero) in the fluid due to both the accelerating effect of rotating wall and decelerating effect of static wall through the action of viscous force, and thus the rotational speed of fluid cannot reach that of the driving wall. Furthermore, comparing the inner-wall rotating mode with the outer-wall rotating mode, the former has the smaller driving area and the larger stagnation area, leading to the smaller rotational speed of fluid.

Meanwhile, the simulated SGV volume of the third driving mode i.e. the dual-wall rotating mode are very close to that of the SGV formation theory, which are 1.27 m^3 and 1.23 m^3 respectively. Thus, the dual-wall rotating mode is

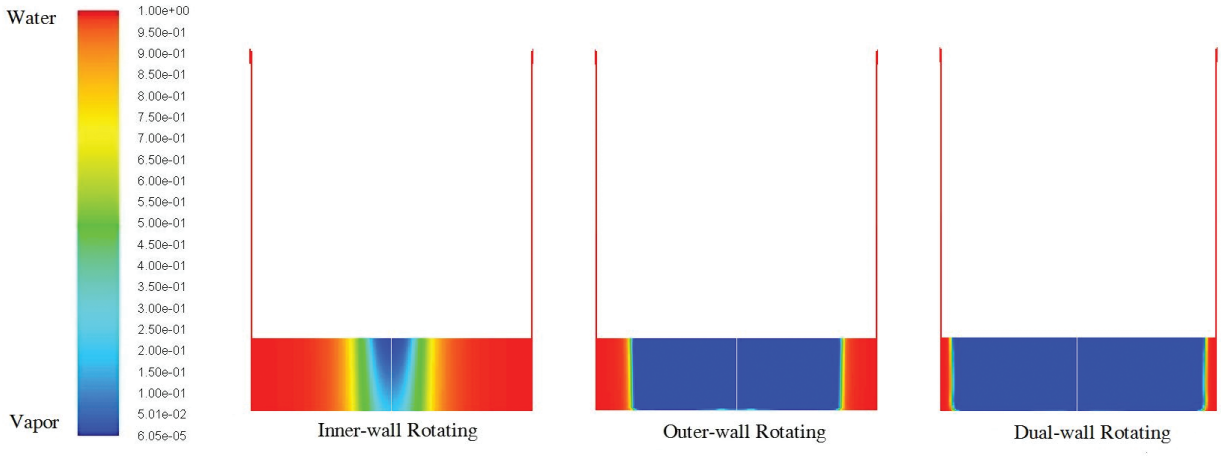

Fig. 3. Volume fraction of water at three different driving modes. R_O = 1.0 m, p_R = 60 kPa, ω = 30 rad/s, and L = 0.02 m.

screened out to be the best practical mean for the SGV region formation. In this case, the inner and outer walls can be designed as an integrated structure and the feasibility of this mode will be experimentally verified in the following part.

3.2.2. Primary parameter influences

According to the theory of SGV formation, four key parameters have influence on volume of SGV region, which are the outlet pressure p_R, the diameter of outer wall R_O, the rotational speed ω, and the evaporation chamber height H. Meanwhile, to effectively obtain the low pressure region, the z coordinate of overflow weir height must be greater than z_O to provide a liquid seal preventing the air slipping into the super gravity vacuum region from the outlet. Fig. 4 shows the influences of these key parameters on the SGV region volume at the dual-wall rotating mode, comparing with the theoretical calculation results as well, in which the superscript "T" and "S" represents the results from theoretical calculation and CFD simulation respectively. Setting z_O equals to H_Y plus H in all the geometrical models, the simulated SGV region and the parameter influences have good agreement with the theoretical results. Thus, it is proved again that the dual-wall rotating mode is suitable for SGV formation.

In practice, adjustment of these parameters following the above parameter influence rules could increase the SGV region volume or enlarge the low pressure range, but some practical limitations should also be taken into account. Excessively decrease p_R will greatly increase the energy consumption while weakening the advantages of SGVF technique. For z_O increases with the R_O and ω, the increase of R_O and ω will cause the size especially the height of equipment be increased significantly, which increases the difficulty of not only liquid seal, but also dynamic balance, reducing the stability, and reliability of the equipment operation. Thus special attention should be given when elevating R_O and ω either in design and operation.

4. Experiments and discussions

4.1. Equipment and instruments

According to CFD simulation results, the most effective driving mode is the dual-wall rotating mode. To verify this

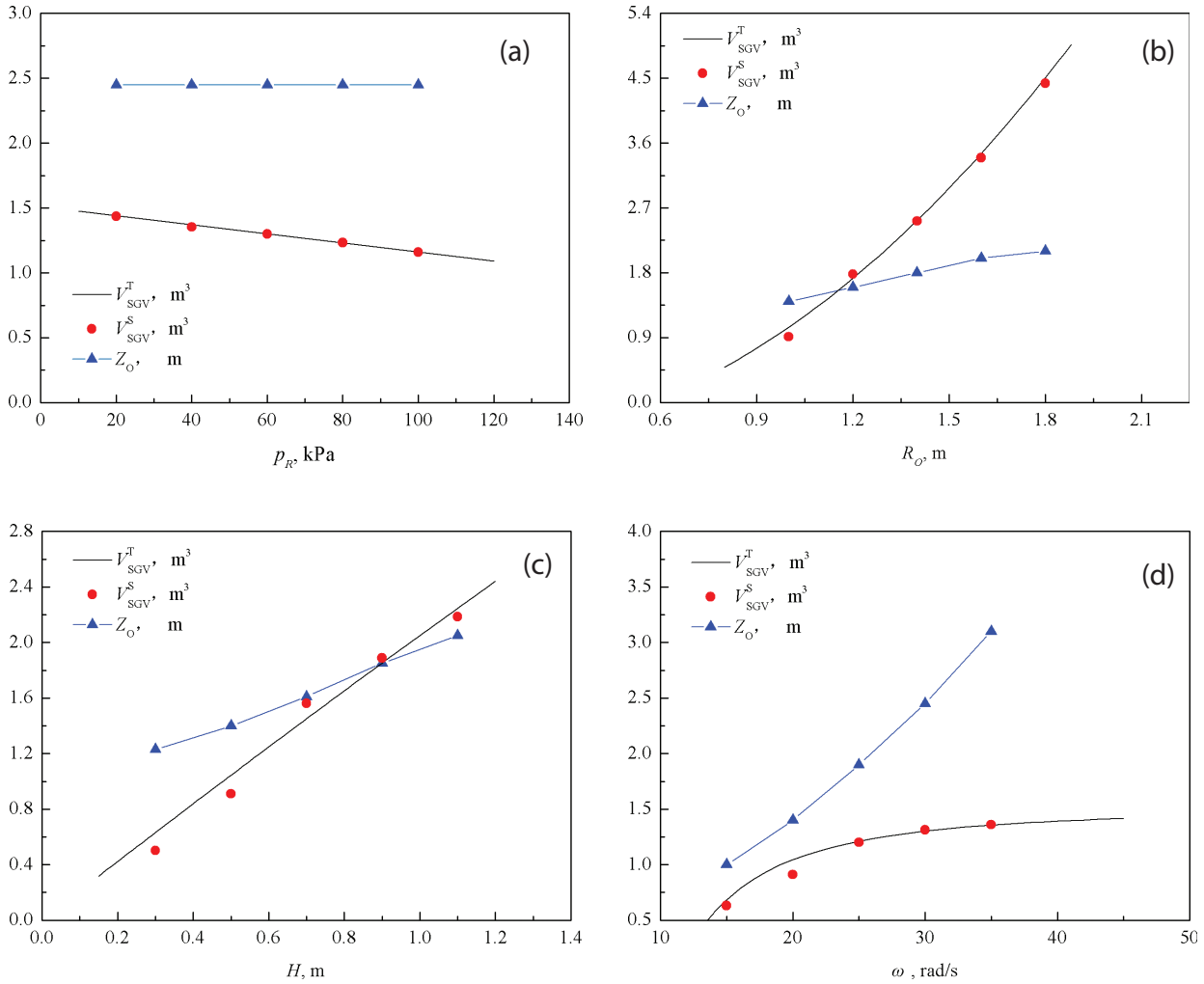

Fig. 4. Parameter influence comparisons, between CFD simulations at the dual-wall rotating mode and the calculation results according to SGV formation theory. (a) p_R, (b) R_O, (c) H, and (d) ω.

driving scheme experimentally, a SGVE with an inner-outer wall integrated structure and driven by a motor is designed and necessary devices and instruments are fully equipped. The composition of the test platform is shown schematically and physically in Figs. 5 and 6 respectively. The test platform comprises an isolation chamber, a SGVE, a vacuum pump, and other necessary adjusting and testing instruments.

The isolation chamber is kept stationary and consists of a base, a cylinder, a cover plate, a dynamic balance plate, and a guiding gutter. The base made of cast iron is fixed to the ground through the anchor bolts to ensure the stability of the equipment during operation. The cylinder and the cover plate which are made of PMMA and engineering plastic ABS respectively, are designed according to the requirements of the external pressure vessel, to guarantee no destabilization occurs under operating pressure. The dynamic balance plate is composed of elastic rubber wheels that are evenly distributed in the circumferential direction, maintaining stability of SGVE during rotation while reducing the frictional resistance through the wheel rolling. The guiding gutter is used to receive and hold the water thrown off from the outflow weir of SGVE, with an outlet being set below and connected to the water storage tank placed in the isolation chamber through pipes.

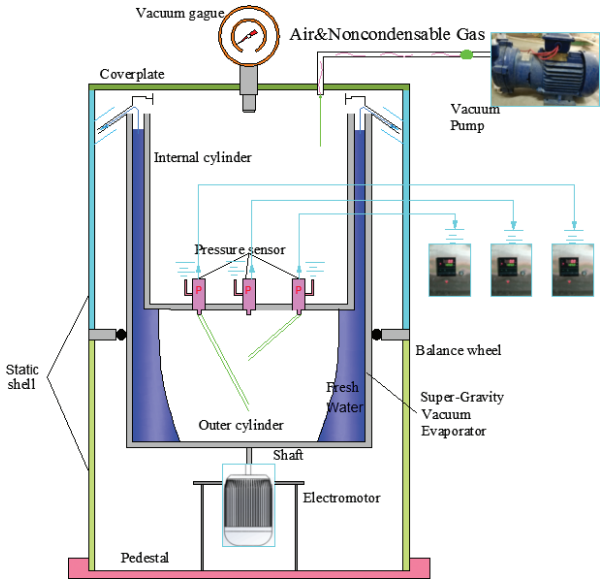

Fig. 5. Schematic of the test platform.

Fig. 6. Photo of the test platform.

The SGVE is coaxially installed in the isolation chamber, and driven by the motor mounted below. There is no need to worry about the space for the installation of electromotor, since the diameter of the super-gravity vacuum evaporator is much greater than that of the electromotor and the vertical space for motor installation and the height of the super-gravity vacuum evaporator can be adjusted according to the height of the electromotor. The overflow weir is provided with a freshwater outlet and non-contact with the gutter, facilitating freshwater overflow. The specific structural parameter of the SGVE is as follows: R_O = 0.286 m, L = 0.011 m, H = 0.271 m, and H_Y = 0.660 m.

In order to obtain a wide range of experimental data, Cima motor with rated power of 3 kW, rated speed of 750 rpm is adopted to drive the SGVE, with the Siemens inverter to adjusting operating rotational speed of motor. A water ring vacuum pump with rated power of 0.81 kW is used to maintain a certain vacuum degree in the isolation chamber. The actual rotational speed of the SGVE is measured by a tachometer (testo 407) and the vacuum degree in the isolation chamber by a vacuum gauge. The absolute pressure at the axis of the SGVE is gauged by wireless pressure sensors (as shown in Fig. 6) with power supply by a built-in battery, transmitted outside to the external receiving modular and displayed on LED screens. Two test points of pressure are set along the axis of SGVE, and their distances from the baseplate of inner cylinder H_t are 0cm and 20 cm respectively. The actual power consumption due to the rotation of SGVE is calculated from the measured data of a kilowatt-hour meter during a fixed time period.

4.2. Results and discussions

4.2.1. Formation of super-gravity low-pressure region

Since the structural parameters of the SGVE are given, the changeable parameters left in the experiments are only the operating parameters.

Defining a non-dimensionalized quantity Ω by Eq. (9) to indicate the vacuum extent of the super-gravity low-pressure region, where p is the absolute pressure and p_0 is the local atmospheric pressure.

$$\Omega = \frac{p}{p_0} \tag{9}$$

Then, the vacuum extent at the SGVE outlet and monitored in the super-gravity low-pressure region can be represented by Ω_R and Ω_{SG} respectively. The adjusting range of outlet vacuum extent Ω_R is 0.5 to 1.0, and the rotational speed of SGVE ω can vary in the range of 200 to 375 r/min.

Fig. 7 shows the variation of Ω_{SG} with time, from starting up to the rotational equilibrium state. Driven by

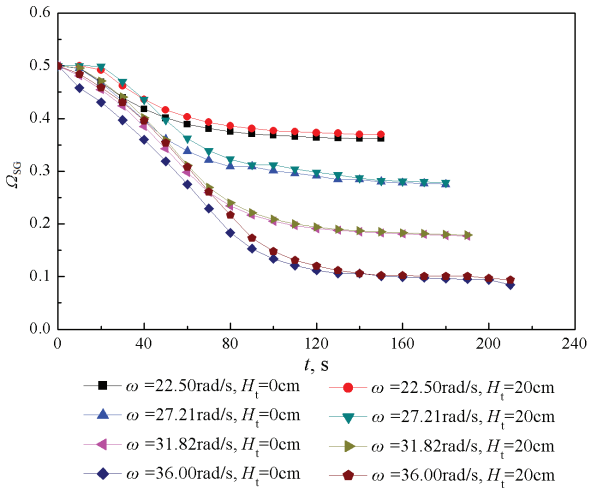

Fig. 7. Variation of Ω_{SG} with time, from starting up to the rotational equilibrium state.

SGVE, the interior water is accelerated and the pressure in fluid domain decreases. When the tested Ω_{SG} approaches a constant, the interior water flow is close to the rotational equilibrium state, indicating that the designed equipment is operated stably as well. The required time to achieve the equilibrium state increases with ω, and for all operating conditions it is no more than 2 min, indicating that 2 min is enough for the startup of SGVE.

Fig. 8 shows the variation of Ω_{SG} with ω and p_R ((a) $H_t = 0$; (b) $H_t = 20$ cm), where the theoretical value of vacuum extent is calculated based on the Eq. (10). According to the SGV formation theory, setting $r = 0$, and $z = H–H_t$, where p_T and p_R are the theoretical absolute pressure in the super-gravity low-pressure region and the absolute pressure at the SGVE outlet respectively.

$$p_T = p_R - \rho\frac{\omega^2}{2}\left(R_o^2 - r^2\right) + \rho g\left(z_o - z\right) \quad (10)$$

The experimental test results are in good agreement with the theoretical predictions proving that it is feasible to obtain a super-gravity low pressure environment by rotating the SGVE with integrated inner-outer wall structure, i.e. by the dual-wall rotating mode. With the increase of ω and the decrease of p_R, Ω_{SG} decreases significantly. Under the same operation conditions, the pressure gauged at location ($r = 0$, $z = 0.271$ m) is a little less than that at location ($r = 0$, $z = 0.251$ m) for the action of gravity force.

4.2.2. Rotational speed slip

Nearly all the test data are greater than the corresponding theoretical predictions and their difference become more obvious with the increase of ω, indicating that a rotational speed slip existing between the walls of SEVE and the interior water flow, which should be taken into account in the both design and operation of SGVE hereafter. Replacing p_T with p_E (the gauged absolute pressure in the super-gravity low-pressure region) in Eq. (10), the actual rotational speed

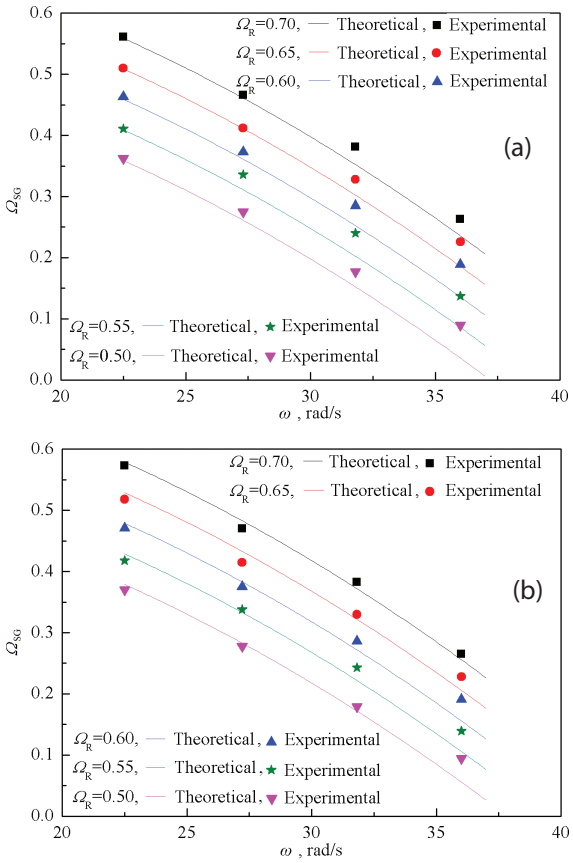

Fig. 8. Variation of Ω_{SG} with ω and p_R. (a) $H_t = 0$, and (b) $H_t = 20$ cm.

of interior water flow can be calculated, based on which, the relative rotational speed slip Δω/ω can be obtained. In Fig. 9, the variation of the relative rotational speed slip Δω/ω with the rotational speed of SGVE ω is shown. With the increase of ω, the rotational speed slip grows up too, and within the operating range, the relative rotational speed slip can be controlled within 6%.

Some inserted structure could help water to move together with the wall better. For the limitation of the desalination space, the inserted structure should not only have the function of keeping water move together with the wall, but also have the function of desalinating water. After the successful acquisition of the super-gravity low-pressure region, our work will continue to focus on the implementation of seawater desalination in this region in the near future, and correspondingly there will be some necessary desalinating structures inserted into the super-gravity low-pressure region simultaneously offering much more driving walls for water to alleviate the velocity slip issue.

4.2.3. Energy consumption

Energy consumption is also an important factor for the application of the SGV technique into desalination. During the operation of SGVE, the energy consumers include the motor which used to drive the SGVE and the vacuum pump. The vacuum pump is running mainly at the start-up phase lasting only about 5 min, and running occasionally during

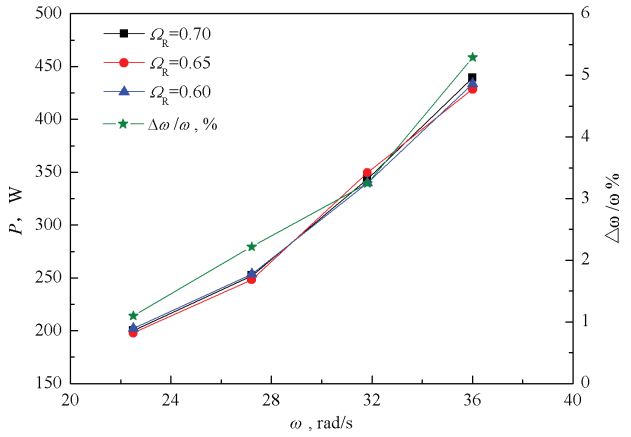

Fig. 9. Variation of relative rotational speed slip and consumed power of SGVE with ω.

the experiment due to the low demand of vacuum degree and the good sealing of the isolation chamber. Therefore, the energy consumption is mainly caused by the rotation of the SGVE motor. Fig. 9 shows the variation of consumed power of SGVE motor with ω and p_R. The energy consumption increases remarkably with ω. With the increase of ω, the resistances caused by friction between the outer-wall of SGVE and the balancing wheel, and between the shaft and bearings are both enhanced, leading to the increase of driving power. The test results show that when ω reaches at the maximal testing rotational speed, 36.11 rad/s, the pressure of the super-gravity low pressure region decreasing to 8.9 kPa, the consumed power is about 425 W.

The tested power consumption caused by the operation of SGVE (the device for generating the super-gravity vacuum/low pressure circumstance) is very small. Meanwhile, since the vacuum/low-pressure circumstance is not directly obtained by vacuum pump, the auxiliary vacuum pump load can be decreased effectively for the decreasing demand in the vacuum extent. Thus, as a component of the seawater desalination process, SGVE will cause little extra energy consumption to the entire process, and has good prospect to be integrated with the available technologies of desalination.

4.2.4. Feasibilities of SGV evaporator combined with membrane distillation for desalination enhancement

The investigated practical mean is for the formation of the super-gravity vacuum/low-pressure circumstance which is a necessary precondition for the seawater desalination. The formed vacuum/low-pressure circumstance needs to be combined with the traditional thermal desalination process or membrane distillation to achieve the seawater desalination. In this part, the possibilities of integrating SGVE into the available desalination technologies will be discussed.

Limited to the laboratory height which is unable to meet the height requirement of the overflow weir, the SGV vapor region is not obtained during the experiment. When the absolute pressure of the isolation chamber is 50 kPa, the absolute pressure in the super-gravity low pressure region can reach 8.9 kPa with a decrease of 81.4%, which is in the same order of the saturated vapor pressure of the ambient temperature. In this case, the super-gravity low pressure region is full of low pressure liquid water and thus cannot be integrated with the thermal desalination technology such as the vacuum distillation. However, in virtue of hydrophobic permeable membranes as an interface of seawater and freshwater, the above low-pressure environment can be also employed for seawater desalination. The desalination process is much like a VMD (vacuum membrane distillation) [32–34], with the following differences: (1) The vacuum/low-pressure environment to speed up the evaporation of seawater and the transmission of vapor is created by SGV technique but not just the vacuum pump; (2) The vacuum/low-pressure region is filled with fresh water with low-pressure and high rotational speed. Thus, the desalination process can be enhanced through a combination of SGVE with MD.

The membrane module consisting of several membrane-covered tubes is immersed in the super-gravity low-pressure region of SGVE and rotates together with the SGVE. By a specially designed inner structure of the tube, the atomization and evaporation of seawater occurs in the tube, i.e. on the one side of the membrane, the vapor transfers across the membrane and condenses out of the tube, i.e. on the other side of the membrane which is directly contacted with the fresh water. For the obvious pressure difference between the two sides of the membrane, the distillation of seawater is similar to the VMD, and thus the membrane flux could be effectively elevated. For there is no direct contact between the seawater flow and the membrane, the wetting, fouling, and scaling of the membrane could be effectively alleviated, which are the main limitations for application of VMD and cause various difficulties in membrane preparation [35–37]. As to the energy consumption of the SGVE-MD process (the combination of SGVE and MD), it can be predicted as the summation of the energy consumption of SGVE and MD [38], below (1.75 + 0.5) kWh/m^3, which is similar to that of the commercial RO technique (2 to 4 kWh/ m^3) [39,40].

Therefore, the SGVE-MD process can avoid the mixing of seawater with fresh water in the super-gravity low-pressure region, effectively adopt the low pressure environment for desalination enhancement, refrain from the disadvantages of VMD and meanwhile has competitive energy consumption with the commercial RO technique, having good prospect in the seawater desalination field.

5. Conclusions

Based on the previous conceptual process design and theoretical analysis of SGVF technique, the practical means for the formation of SGV or low pressure region are discussed in this paper. By analyzing the characteristics of the fluid field necessary for SGV formation, three driving mode are proposed, which are the inner-wall rotating mode, the outer-wall rotating mode, and the dual-wall rotating mode.

To screen out the most effective driving mode for SGV formation, the 3D flow field of the SGV formation is simplified to a 2D axisymmetric rotating model, based on which the CFD model is established including governing equations, boundary conditions, and the solution strategies. The simulated results show that the most effective mode for SGV formation is the dual-wall rotating mode at which the simulation data and parameter influences have good agreement

with the theoretical calculations. Also, based on the simulation results, some advices for SGVE design and operation are proposed.

To verify the dual-wall mode being a suitable practical mean for the SGV formation, a test platform is set up, including a SGVE driven by a motor, a vacuum pump, an isolation room, and other necessary devices and measuring instruments. The pressure drop during the formation of the super-gravity low pressure region is investigated, with the obtained parameter influences in good consistence with the simulating and theoretical results. Under the experimental conditions, the minimal absolute pressure in the super-gravity low pressure region can achieve 8.9 kPa, which is in the same order as the saturated pressure of water at ambient temperature.

The tested power consumption caused by the operation of SGVE (the device for generating the super-gravity vacuum/low pressure circumstance) is very small. Meanwhile, since the vacuum/low-pressure circumstance is not directly obtained by vacuum pump, the auxiliary vacuum pump load can be decreased effectively for the decreasing demand in the vacuum extent. Thus, as a component of the seawater desalination process, SGVE will not cause extra energy consumption to the entire process, and has good prospect to be integrated into the available technologies of desalination.

Based on above simulating and experimental studies, a novel desalination process, SGVE-MD is proposed, with both advantages of SGVF and MD while refraining from their disadvantages. This process has a good perspective in seawater desalination and renewable energy utilization, and will be further studied.

Acknowledgement

The financial supports by the National Natural Science Foundations of China (51769006), and the Central Government Guiding Special Funds for the Development of Local Science and Technology (ZY2018HN09–6) are gratefully acknowledged.

References

[1] FAO, Coping with water scarcity in agriculture: a global framework for action in a changing climate, 2016.
[2] F. Macedonio, E. Drioli, A.A. Gusev, A. Bardow, R. Semiat, M. Kurihara,. Efficient technologies for world clean water supply, Chem. Eng. Process., 51 (2012) 2–17.
[3] V.V. Rosen, O.G. Garber, Y. Chen, Magnesium deficiency in tap water in Israel: the desalination era, Desalination, 426 (2018) 88–96.
[4] M.A. Abdelkareem, M.E.H. Assad, E.T. Sayed, B. Soudan, Recent progress in the use of renewable energy sources to power water desalination plants, Desalination, 435 (2018) 97–113.
[5] H.B. Harandi, M. Rahnama, E.J. Javaran, A. Asadi, Performance optimization of a multi stage flash desalination unit with thermal vapor compression using genetic algorithm, Appl. Therm. Eng., 123 (2017) 1106–1119.
[6] M. Monnot, H.T.K. Nguyen, S. Laborie, C. Cabassud, Seawater reverse osmosis desalination plant at community-scale: role of an innovative pretreatment on process performances and intensification, Chem. Eng. Process., 113 (2017) 42–55.
[7] IDE's desal plant in Ashkelon, Israel sets world record, Pump Industry Analyst, 2015 (2015) 3–4.
[8] M.L. Elsayed, O. Mesalhy, R.H. Mohammed, L.C. Chow,, Transient performance of MED processes with different feed configurations, Desalination, 438 (2018) 37–53.
[9] F. Galvanin, R. Marchesini, M. Barolo, F. Bezzo, M. Fidaleo, Optimal design of experiments for parameter identification in electrodialysis models, Chem. Eng. Res. Des., 105 (2016) 107–119.
[10] M. Qasim, F. Mohammed, A. Aidan, N.A. Darwish, Forward osmosis desalination using ferric sulfate draw solute., Desalination, 423 (2017) 12–20.
[11] L. Zheng, J. Wang, J. Li, Y. Zhang, K. Li, Y. Wei, Preparation, evaluation and modification of PVDF-CTFE hydrophobic membrane for MD desalination application, Desalination, 402, (2017) 162–172.
[12] A. Hagedom, G. Fieg, D. Winter, J. Koschikowski, T. Mann, Methodical design and operation of membrane distillation plants for desalination, Chem. Eng. Res. Des., 125 (2017) 265–281.
[13] R. Santosh, T. Arunkumar, R. Velraj, G. Kumaresan, Technological advancements in solar energy driven humidification-dehumidification desalination systems - A review, J. Clean Prod., 207 (2019) 826–845.
[14] M. Saleem, W. Kim, Parameter-based performance evaluation and optimization of a capacitive deionization desalination process, Desalination, 437 (2018) 133–143.
[15] H. Fakharian, H. Ganji, A. Naderifar, Desalination of high salinity produced water using natural gas hydrate, J. Taiwan Inst. Chem. E., 72 (2017) 157–162.
[16] B. Kalista, H. Shin, J. Cho, A. Jang, Current development and future prospect review of freeze desalination, Desalination, 447 (2018) 167–181.
[17] N. Ghaffour, TM Missimer, GL. Amy, Technical review and evaluation of the economics of water desalination: current and future challenges for better water supply sustainability, Desalination, 309 (2013) 197–207.
[18] International Desalination Association., Market Profile 2016–2017, 2017. Desalination Yearbook.
[19] M.W. Shahzad, M. Burhan, L. Ang, K.C.Ng, Energy-water-environment nexus underpinning future desalination sustainability, Desalination, 413 (2017) 52–64.
[20] A. Alkaisia, R. Mossad, A. Sharifian-Barforoush, A review of the water desalination systems integrated with renewable energy, Energy Procedia, 110 (2017) 268–274.
[21] M. Shatat, M. Worall, S. Riffat, Opportunities for solar water desalination worldwide: review, Sustain. Cities Soc., 9 (2013) 67–80.
[22] A. Madhlopa, D. Sparks, S. Keen, M. Moorlach, P. Krog, T. Dlamini,. Optimization of a PV–wind hybrid system under limited water resources, Renew. Sust. Energ. Rev., 47 (2015) 324–331.
[23] J.A. Carta, J. González, P. Cabrera, V.J. Subiela, Preliminary experimental analysis of a small-scale prototype SWRO desalination plant, designed for continuous adjustment of its energy consumption to the widely varying power generated by a stand-alone wind turbine, Appl. Energ., 137 (2015) 222–239.
[24] M. Smaoui, A. Abdelkafi, L. Krichen, Optimal sizing of stand-alone photovoltaic/ wind/hydrogen hybrid system supplying a desalination unit, Sol. Energy, 120 (2015) 263–276.
[25] D. Zejli, A. Ouammi, R. Sacile, H. Dagdougui, A. Elmidaoui, An optimization model for a mechanical vapor compression desalination plant driven by a wind/PV hybrid system, Appl. Energ., 88 (2011) 4042–4054.
[26] A. Midilli, Waste water distillation via natural vacuum technique. Turkey: Karadeniz Technical University, 1997.
[27] S. Al-Kharabsheh, D.Y. Goswami, Analysis of an innovative water desalination system using low-grade solar heat, Desalination, 156 (2003) 323–332.
[28] S. Al-Kharabsheh, D.Y. Goswami, Experimental study of an innovative solar water desalination system utilizing a passive vacuum technique, Sol. Energy, 75 (2003) 395–401.
[29] Q. Ma, C. Yi, H. Lu, L. Xie, J. Fan, W. He, A conceptual demonstration and theoretical design of a novel"super-gravity" vacuum flash process for seawater desalination, Desalination, 371 (2015) 67–77.
[30] B.E. Launder, D.B. Spalding, The Numerical Computation of Turbulent Flows, Comput. Method. Appl. M., 3 (1974) 269–289.

[31] A.K. Singhal, H.Y. Li, M.M. Athavale, Y. Jiang, Mathematical Basis and Validation of the Full Cavitation Model, ASME FEDSM'01, New Orleans, Louisiana, 2001.
[32] A. Rom, W. Wukovits, F. Anton, Development of a vacuum membrane distillation unit operation: from experimental data to a simulation model, Chem. Eng. Process., 86 (2014) 90–95.
[33] J. Liu, Q. Wang, L. Han, B. Li, Simulation of heat and mass transfer with cross-flow hollow fiber vacuum membrane distillation: the influence of fiber arrangement, Chem. Eng. Res. Des., 119 (2017) 12–22.
[34] W. Cao, Q. Liu, Y. Wang, L.M. Mujtaba, Modeling and simulation of VMD desalination process by ANN, Comput. Chem. Eng., 84 (2016) 96–103.
[35] Q.F. Alsalhy, S.S. Ibrahim, S.R. Khaleel, Performance of vacuum poly (propylene) membrane distillation (VMD) for saline water desalination, Chem. Eng. Process., 120 (2017) 68–80.
[36] D. Chen, N. Li, J. Zhang, Modeling and multi-objective optimization of vacuum membrane distillation for enhancement of water productivity and thermal efficiency in desalination, Chem. Eng. Res. Des., 132 (2018) 697–713.
[37] M. Baghbanzadeh, D. Rana, C.Q. Lan, T. Matsuura, Effects of hydrophilic silica nanoparticles and backing material in improving the structure and performance of VMD PVDF membranes, Sep. Purif. Technol., 157 (2016) 60–71.
[38] G. Dong, J.F. Kima, J.H. Kima, E. Drioli, Y.M. Lee, Open-source predictive simulators for scale-up of direct contactmembrane distillation modules for seawater desalination, Desalination, 402, (2017) 72–87.
[39] Y. Zhao, Z. Zhanga, L. Daia, H. Maoa, S. Zhanga, Enhanced both water flux and salt rejection of reverse osmosis membrane through combining isophthaloyl dichloride with biphenyl tetraacyl chloride as organic phase monomer for seawater desalination, J. Membr. Sci., 522 (2017) 175–182.
[40] R.K. McGovern, V.J.H. Lienhard, On the asymptotic flux of ultrapermeable seawater reverse osmosis membranes due to concentration polarization, J. Membr. Sci., 520 (2016) 560–565.